CRYSTAL GROWTH & DESIGN

Article

Cite This: *Cryst. Growth Des.* 2018, 18, 4320−4333

pubs.acs.org/crystal

ATP Induced Modulation in π−π Stacking Interactions in Pyrene Based Zinc Complexes: Chemosensor Study and Quantitative Investigation of Apyrase Activity

Published as part of a Crystal Growth and Design virtual special issue on π−π Stacking in Crystal Engineering: Fundamentals and Applications

Amanpreet Singh,[†] Pushap Raj,[†] Jan J. Dubowski,[‡] and Narinder Singh*[,†]

[†]Department of Chemistry, Indian Institute Technology Ropar, Punjab, 140001, India

[‡]Laboratory for Quantum Semiconductors and Photon-Based BioNanotechnology, Interdisciplinary Institute for Technological Innovation (3IT), CNRS UMI-3463, Department of Electrical and Computer Engineering, Université de Sherbrooke, 2500 boul. de l'Université, Sherbrooke, Québec J1K 2R1, Canada

Supporting Information

ABSTRACT: Fluorescent zinc complexes of 1,2-disubstituted benzimidazole (**R1**−**R3**) have been synthesized and characterized using single crystal X-ray diffraction. The ligands **L1**−**3** were found to be less emissive due to photoinduced electron transfer (PET) mechanism originated from the electron pair of benzimidazole nitrogen. The complexation of ligands with Zn(II) not only enhances the fluorescent intensity; it also orients the ligands to a new packing. It was observed that the aromatic unit plays a decisive role in the packing of the molecules. The complex **R1** has extended the coordination through C−H···π interaction, whereas complex **R2** involved C−H···π interaction and C−H···Br interaction for packing in supramolecular architecture. Among these complexes, **R3** showed the most interesting noncovalent interaction pattern involving C−H···π interaction, C−H···Br interaction, and π−π stacking between pyrene rings. These noncovalent interactions govern photophysical properties that are sensitive toward the microenvironment. Thus, by altering these interactions, the selective sensing for a particular analyte can be achieved. The complexes **R1** and **R2** have shown enhanced emission intensity upon interacting with adenosine triphosphate (ATP) competitively in the presence of some other tested anions. A ratiometric change in emission spectra of the complex **R3** was observed upon binding with ATP in semiaqueous medium offering the lowest detection limit of 15 nM. Upon interaction with ATP, the π−π stacking between pyrene rings breaks and results in a decrease in excimer emission at 470 nm and increases in monomeric emission intensity at 410 nm. The AFM (Atomic force microscopy) images of receptor **R3** show that upon addition of ATP to the **R3** solution, solvent mediated aggregation takes place, which results in the ratiometric detection. In the dimethylformamide solvent system, aggregates were formed, whereas in a water/tetrahydrofuran solvent system the clear solution was converted to a highly viscous gel. To investigate the applications of the prepared sensor, the fluorescence response of HeLa cells enriched with ATP was observed using fluorescence microscopy. The fluorescence modulation of the sensor in living cells makes the receptor practically applicable in a biological environment. Quantitative analysis of apyrase activity has shown that the presented sensor **R3** is capable of monitoring the hydrolysis process in the biological system.

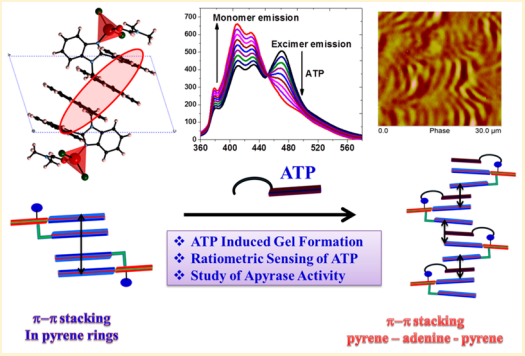

INTRODUCTION

Detection of anionic species in aqueous medium becomes an imperative goal for supramolecular chemistry because these are pervasive in biological systems and an play important role in environmental monitoring and diagnosis.[1−5] Unlike cations, anionic species have different shapes and sizes, and hence anionic biomolecules require complementary receptors to encapsulate.[6−9] The biologically important anionic species such as phosphates and nucleic bases due to their diverse sizes and shapes demand a receptor design, which is sometimes tedious to develop using synthetic skills. The literature reports reveal the synthesis of organic receptors that can detect analytes through anion induced fluorescence modulations.[10,11] Most of these organic receptors are fabricated of urea/thiourea groups or imidazolium organic cations.[12−15] The rationale of insertion of urea/thiourea in the receptor design lies with the fact that these moieties have a tendency to form hydrogen bonds with anionic analytes. However, on the other hand, it

Received: January 31, 2018
Revised: May 15, 2018
Published: June 20, 2018

DOI: 10.1021/acs.cgd.8b00165
Cryst. Growth Des. 2018, 18, 4320−4333

Table 1. Crystal Data and Structure Refinement

CCDC no.	1526966	1526967	1526968
identification code	(**R1**)	(**R2**)	(**R3**)
empirical formula	$C_{40}H_{32}Br_2N_4Zn$	$C_{31}H_{27}Cl_2N_3OZn$	$C_{43}H_{31}Br_2N_3OZn$
formula weight	793.93	593.88	830.95
temperature/K	298.0	298.0	298.0
crystal system	monoclinic	monoclinic	triclinic
space group	$C2/c$	$P2_1/c$	$P\bar{1}$
a/Å	19.0112(11)	11.6647(4)	9.0618(3)
b/Å	10.6875(5)	13.5988(4)	13.0320(5)
c/Å	18.8991(12)	17.5829(6)	16.0651(6)
α/°	90	90	100.320(2)
β/°	116.307(6)	94.2986(10)	105.531(2)
γ/°	90	90	98.173(2)
volume/Å^3	3442.3(4)	2781.26(16)	1761.79(11)
Z	4	4	2
ρ_{calc}, g/cm^3	1.5318	1.4182	1.5663
$F(000)$	1599.5	1226.8	835.8
crystal size/mm^3	0.5 × 0.4 × 0.4	0.5 × 0.4 × 0.4	0.28 × 0.2 × 0.16
radiation	Mo Kα (λ = 0.71073)	Mo Kα (λ = 0.71073)	Mo Kα (λ = 0.71073)
2Θ range for data collection/°	4.5 to 56.86	4.6 to 56.54	4.68 to 56.62
independent reflections	4308 [R_{int} = 0.1005, R_{sigma} = 0.0884]	6886 [R_{int} = 0.0430, R_{sigma} = 0.0415]	8730 [R_{int} = 0.0474, R_{sigma} = 0.0467]
data/restraints/parameters	4308/0/212	6886/0/344	8730/0/452
goodness-of-fit on F^2	1.004	0.966	1.042
final R indexes [$I \geq 2\sigma(I)$]	R_1 = 0.0585, wR_2 = 0.1419	R_1 = 0.0416, wR_2 = 0.1207	R_1 = 0.0407, wR_2 = 0.0748
final R indexes [all data]	R_1 = 0.1516, wR_2 = 0.1869	R_1 = 0.0769, wR_2 = 0.1453	R_1 = 0.0855, wR_2 = 0.0884

has been observed that the receptors relying on purely hydrogen bonding have limited application, while working in aqueous medium due to the competition provided to binding site from water, and moreover hydration of anionic species.[16−20] Therefore, the design of a sensor for biomolecules, particularly in an aqueous medium, is still a challenge to inorganic-analytical chemistry. Among these biomolecules, adenosine triphosphate (ATP) is one of the most important anions that contain three negatively charged phosphates.[21−23] It enzymatically hydrolyzes in the cell to give adenosine diphosphate (ADP), adenosine monophosphate (AMP), and pyrophosphates.[24,25] Apart from these, it also plays a significant role in DNA replication and transcription. Due to the similarity in structure of various competing species, a selective sensor for ATP is the need of the hour. Selectivity can be modulated (improved) by incorporation of hydrogen bonding interaction, ionic interaction, van der Waals interaction and $\pi-\pi$ interaction into the receptor.[26,27] Along with these interactions, C−H···π interaction and C−H···halide interactions also play a decisive role in the formation of the supramolecular assembly through noncovalent interactions.[28−31] Likewise, $\pi-\pi$ stacking and hydrogen bonding interaction cause the formation of supramolecular self-assembly which results in aggregation formation or gel formation.[32−39] Not only is supramolecular assembly of metal complex engaged by noncovalent interactions, but also their photophysical properties are directed by these weak interactions in solution as well as in the solid state.[40−44] Therefore, by taking advantage of noncovalent interactions, sensitive and selective sensors can be developed. Recently, Maji et al. have developed a selective sensor for Al(III) that responds to Al(III) by fluctuating emission behavior due to change induced by noncovalent interactions.[45] ATP has an adenosine subunit that can interact through $\pi-\pi$ interaction with analytes.[46−48] Similarly three negatively charged phosphate units have a tendency to interact through ionic interaction. In view of this, Yoon et al. had constructed a dipodal receptor that contains pyrene excimer as a signaling unit which upon stacking with adenine gave a change in emission.[49] The imidazolium unit conjugated to pyrene acts as a phosphate ion receptor. The sensor showed ratiometric sensing of ATP; however, some analytes such as AMP and ADP also show some interference. Kataev et al. have synthesized two copper complexes labeled with fluorescent coumarin and anthracene units for detection of ATP in an aqueous medium, which shows some interference due to other analytes.[50] Also, some binuclear complexes have been developed for sensing of ATP, AMP, and pyrophosphates. The two phosphate units coordinate with two different zinc ions, resulting in a change in photophysical properties of the receptor.

In the present work, we have synthesized 1,2 disubstituted fluorescent labeled benzimidazole derivatives (Figure S1) and their complexes with zinc ion. Particularly, the zinc ion was chosen due to its d^{10} configuration, which resists the loss of fluorescence upon complexation due to nonavailability of the open shell effect. The complexes **R2** and **R3** contain two halide ions and one solvent molecule which can be easily replaced by some strong field ligands. The most interesting features of these complexes are their differences in noncovalent interactions, resulting from a change in aromatic unit attached with a benzimidazole moiety. These complexes have the ability to interact with analytes through ionic interaction as well as $\pi-\pi$ stacking. Due to the dual interaction of analyte, ratiometric sensing can be achieved. The ratiometric sensors are more reliable than simply "on−off" fluorescence sensors because the ratiometric behavior is independent from environmental factors, such as temperature, concentration, slit width, and scan rate.[46] To the best of our knowledge, the prepared metal complexes of 1,2 disubstituted benzimidazole are novel, and there is no report on disubstituted benzimidazole based

DOI: 10.1021/acs.cgd.8b00165
Cryst. Growth Des. 2018, 18, 4320−4333

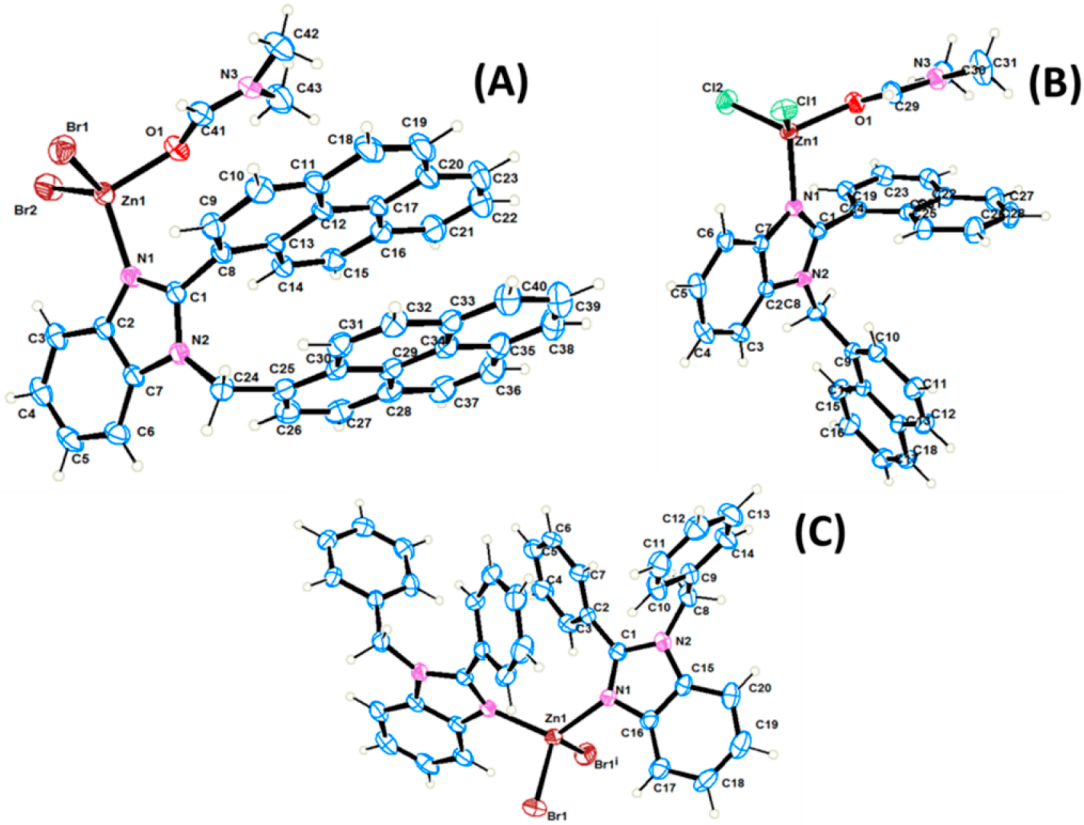

Figure 1. Crystal structure of complex (A) **R1**, (B) **R2**, and (C) **R3** with 40% probability thermal ellipsoids.

sensor for biomolecules. Thus, this system provides a simpler and more effective way to detect ATP than the methods reported in the existing literature.[47−49] The interesting fact about this work is the formation of metallogel upon interaction of **R1** with ATP in tetrahydrofuran (THF)/water (30:70).

RESULTS AND DISCUSSION

Synthesis and Characterization of Ligand and Metal Complex. The ligands **L1** and **L2** were prepared by a reported method from our research group.[51] The ligand **L3** was synthesized through a condensation reaction between 1 equiv of *o*-phenylenediamine and 2 equiv of the corresponding aldehyde in methanol. Characterization of the ligand was achieved using ^{1}H NMR, ^{13}C NMR, and elemental analysis. The ^{1}H NMR signal at 5.8 ppm (singlet) confirmed the formation of the product, as this signal corresponds to aliphatic protons, showing intensity for two protons. Also, a number of protons in the aromatic region of ^{1}H NMR spectra and number of carbons in ^{13}C NMR spectra confirmed the structure of corresponding ligands. The complexes of ligand **L1**−**L3** with the zinc ion were prepared in THF and DMF (90:10). For complex **R1**, 2.0 equiv of **L1** was dissolved in THF along with 1 equiv of zinc bromide. The dark powder was separated out that was dissolved by addition of 10% of dimethylformamide. The reaction mixture was heated for 3 h and then cool down to room temperature. The dark brown colored crystals were separated out after 6 h. The complex **R2** was prepared by reacting 1 equiv of **L2** and 1 equiv of zinc chloride in THF/dimethylformamide (DMF) (90:10). Similarly, complex **R3** was prepared using a similar method, the one which was used for the synthesis of **R2**. All of the complexes were characterized using elemental analysis and infrared spectroscopy. For the final validation of structures, a single crystal structure was obtained, showing 2:1, 1:1, and 1:1 composition of ligand/metal complexes, respectively for **L1**, **L2**, and **L3**.

X-ray Structure Determination. Crystals suitable for X-ray diffraction studies were isolated by the slow evaporation technique in THF/DMF. The crystals [{L1}$ZnBr_2$] (**R1**), [{L2(DMF)}$ZnCl_2$] (**R2**), and [{L3(DMF)}$ZnBr_2$] (**R3**) are quite stable, and therefore data of all crystals were collected at room temperature. Data collection and unit cell parameters are shown in Table 1, whereas the list of bond length and bond angles is presented in Tables S1−S9 respectively in the Supporting Information.[52] The structure was solved with the olex2.solve[52] structure solution program using Charge Flipping and refined with the olex2.refine refinement package using Gauss−Newton minimization. Interestingly, upon changing the number of rings from benzene to naphthalene and pyrene, packing of the crystals changes dramatically. The angle of the plane between benzimidazole ring and another aromatic subunit greatly affects the absorbance and emission profile of complexes. Arguably, the most important feature of this paper concerns observation of the difference in noncovalent interaction resulting from a change in aromatic unit attached with benzimidazole moiety, which plays a decisive role in supramolecular packing as well as photophysical properties.

Effect of Aromatic Subunit Attached with Benzimidazole on Packing of Complexes. The complex **R1** was crystallized in the triclinic crystal system with space group $P\bar{1}$. As shown in the crystal structure (Figure 1), two monodentate ligands form a mononuclear complex containing zinc in a tetrahedral geometry. Another two coordination sites of tetrahedral geometry are occupied with the bromide ion,

DOI: 10.1021/acs.cgd.8b00165
Cryst. Growth Des. 2018, 18, 4320−4333

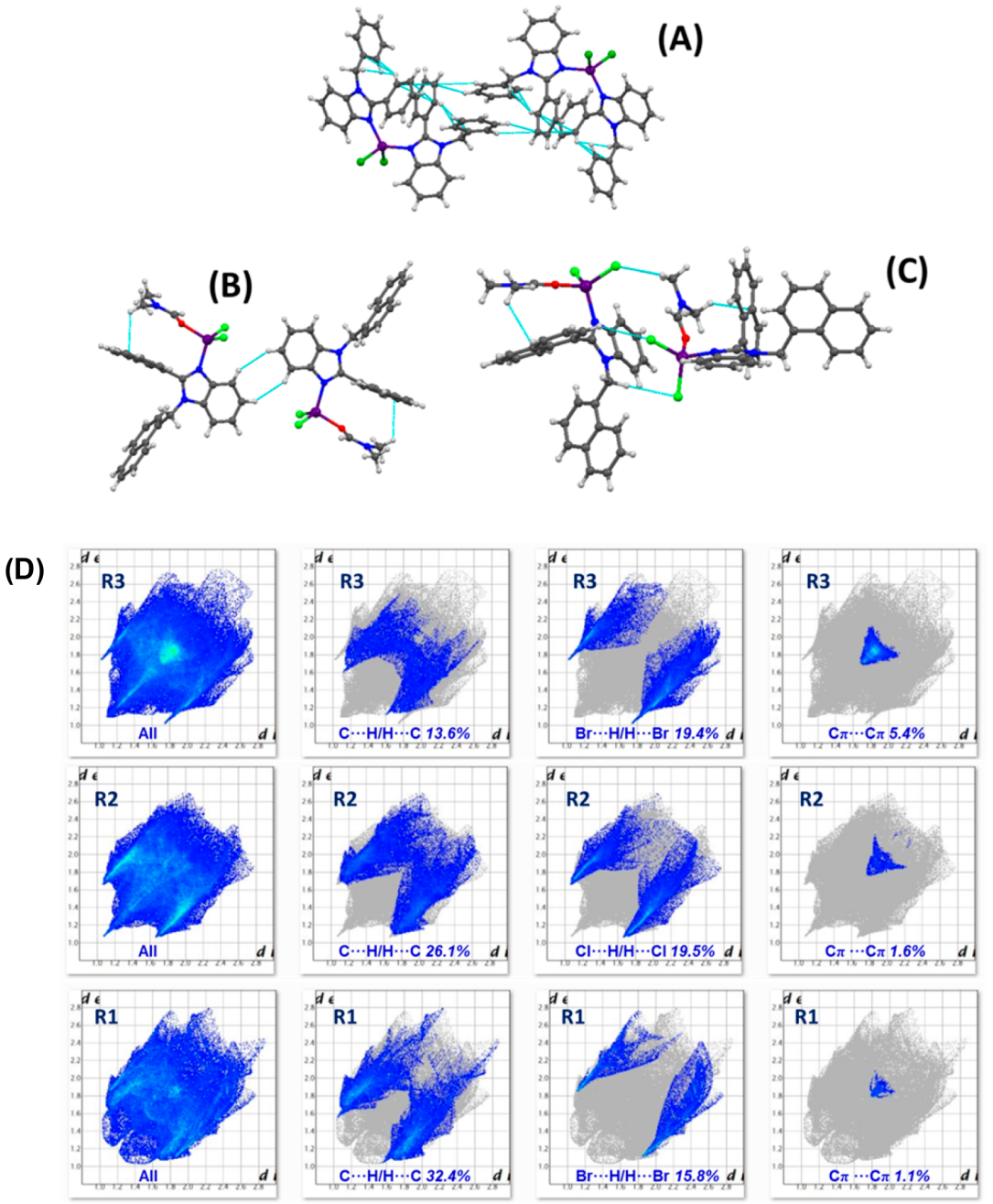

Figure 2. (A) Structural details of **R1**, showing various noncovalent interactions. (B) Structural details of **R2**, showing various noncovalent interactions. (C) C−H···Cl interaction leads to the formation of a polymeric structure in the **R2** complex. (D) Fingerprint plots of the title complex: full and resolved into all, C···H/H···C, X···H/H···X, and Cπ···Cπ contacts showing the percentages of contacts contributed to the total Hirshfeld surface area of molecules.

which also stabilizes the +2 oxidation state of Zn(II). Five different C−H···π interactions gripped different monomeric units into a supramolecular architecture. Only C−H···π interactions were found involved in the construction of the three-dimensional (3-D) supramolecular network. Upon replacement of the benzene ring into the naphthalene ring in complex **R2**, packing of the complex completely changed. Instead of two ligands, only one ligand can coordinate with the zinc ion in **R2**, and a fourth coordination site was occupied by solvent molecule (DMF). As shown in Figure 2, the two monomeric units of complex **R2** hold together through C−H···H−C interaction, whereas the chloride ion interacts with various hydrogens (methylene and aromatic) to extend this 3-D supramolecular architecture. This kind of noncovalent interaction highly depends upon the aromatic π surface, electron-rich or electron-deficient aromatic system.[53,54] The complex **R3** contained a highly conjugated pyrene ring system that has completely different kinds of noncovalent interactions involving $\pi-\pi$ stacking between pyrene rings along with C−H···π and Br···H interactions (Figure 3). These weak noncovalent interactions are highly sensitive toward the microenvironment and play a decisive role in photophysical properties;[55−61] therefore there are reasonable possibilities to develop the sensors for biomolecules. To date, many metal−

DOI: 10.1021/acs.cgd.8b00165
Cryst. Growth Des. 2018, 18, 4320−4333

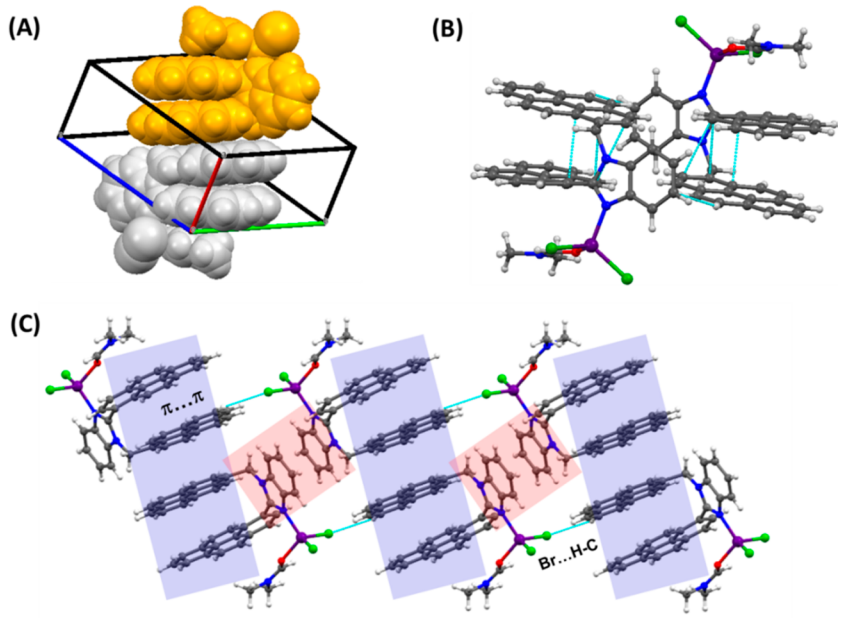

Figure 3. Structural details of **R3**: (a) Interaction between two monomers shown in a space fill model. (b) Intramolecular $\pi\cdots\pi$ stacking interaction between pyrene rings in the **R3** complex. (c) 2D supramolecular layer formed in the *ab* plane.

Table 2. Photophysical Properties of Ligands and Metal Complexes

	λ_{abs} (nm)	ε_0 (L mol^{-1} cm^{-1})	λ_{em} (nm)	λ_{ex} (nm)	quantum yield	τ (ns)	K_r ($\times 10^8$ s^{-1})(average value)	K_{nr} ($\times 10^8$ s^{-1})(average value)
L1	220, 290	4.42×10^4	433	220	0.31	1.1569	3.45	5.64
				290	0.38			
L2	245, 290	4.81×10^4	427, 546	245	0.39	1.2256	3.67	4.67
				290	0.44			
L3	247, 277, 329, 346	5.62×10^4	410, 430, 472	247	0.52	2.1256	2.67	2.10
				277	0.53			
				329	0.55			
				346	0.58			
R1	225, 290	4.65×10^4	433	225	0.48	1.6856	3.38	2.88
				390	0.55			
R2	242, 289	4.85×10^4	427, 546	242	0.51	1.9452	3.11	2.16
				290	0.59			
R3	248, 277, 330, 345	6.61×10^4	410, 430, 472	247	0.73	3.1436	2.45	7.74
				277	0.75			
				329	0.75			
				346	0.76			

organic complexes have been reported with $\pi-\pi$ stacking interactions between the pyrene ring or with another fluorophores.[62−64] However, few reports are available where such kinds of complexes are used for molecular recognition.[65,66] Therefore, to explore the possibility to interact these metal complexes with some particular analytes, molecular recognitions studies were performed with various anionic species using fluorescence spectroscopy. We expected that these specific orientations of metal complexes would introduce interesting photophysical properties that could be altered by the interaction with specific analytes.

To clarify the nature of intermolecular interactions, the Hirshfeld surface of the molecular moiety was analyzed, which provides fingerprint of the interactions involved at the intermolecular level. The Hirshfeld surface mapped with d_{norm} takes various parameters into consideration to calculate normalized contact distance. We have discovered that the major proportion of the Hirshfeld surface was compromised by C···H/H···C interactions in each complex that were the highest in the case of the **R1** complex. The portion of the Hirshfeld surface corresponding to C$\pi\cdots$Cπ increases as the number of aromatic rings increased from benzene to naphthalene and further to pyrene. These results validate the ability of the pyrene ring for the formation of supramolecular self-assembly through $\pi\cdots\pi$ stacking.

Photophysical Properties of Complexes R1 and R2. Initially, spectroscopic properties of ligand **L1** (10 μM) responding to Zn(II) were examined in the HEPES buffer system (pH = 7.0, 1 mM, DMF/water 30:70). Absorbance spectra of **L1** showed two absorbance bands at 225 and 290 nm corresponding to π to π^* and n to π^* transitions, respectively. As displayed in Figure S2, the absorbance intensity of ligand **L1** changes significantly upon addition of the zinc ion.[67,68] To find out the molar excitation coefficient,

DOI: 10.1021/acs.cgd.8b00165
Cryst. Growth Des. 2018, 18, 4320−4333

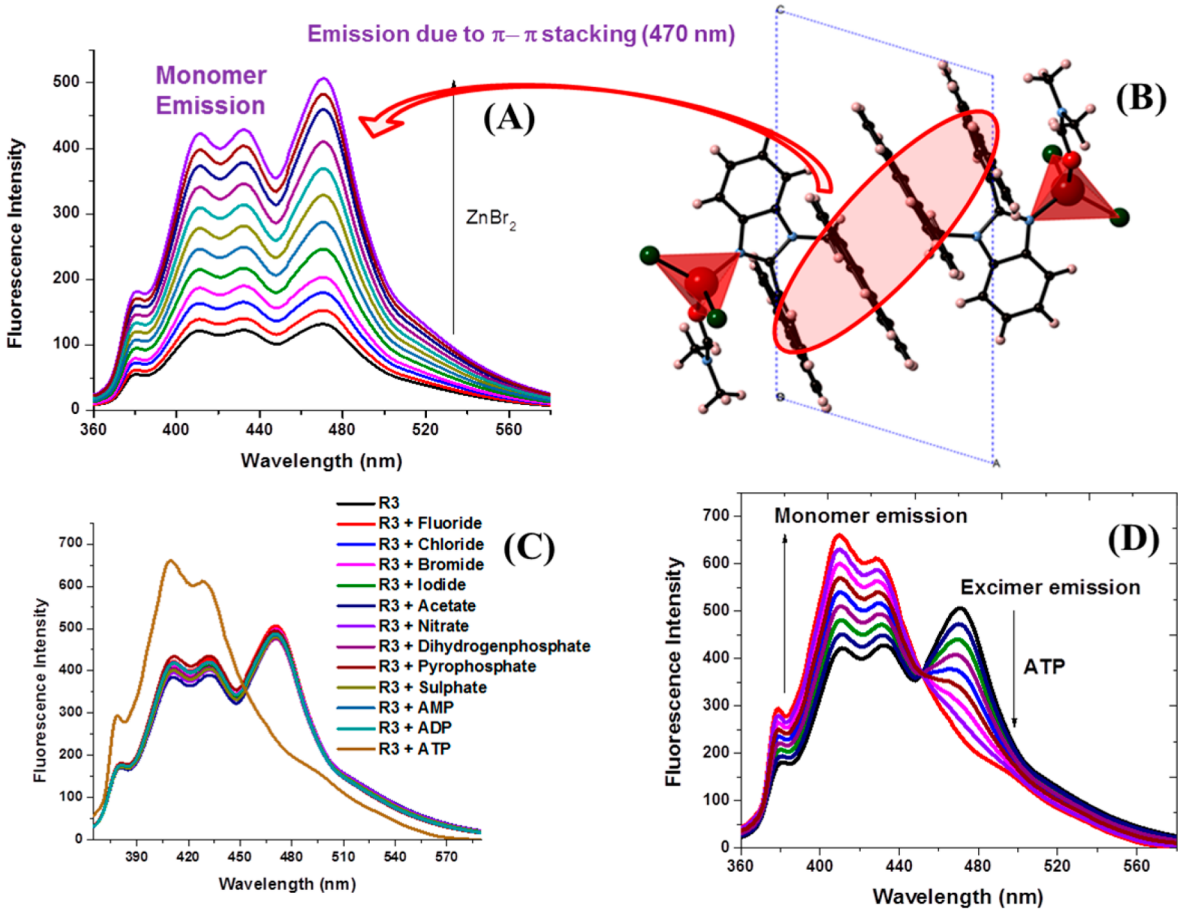

Figure 4. (A) Change in emission profile of ligand **L3** (10 μM) upon addition of 15 μM of zinc bromide in DMF/water (30:70) HEPES buffer. (B) Packing of complex **3**, showing π–π stacking interaction between pyrene rings. (C) Change in emission profile of complex **3** (10 μM) upon addition of 16 μM of various anions in HEPES buffer (DMF/water). (d) Change in emission profile of complex **R3** with successive addition of ATP (0–16 μM).

absorbance was recorded by successive addition of Zn(II) to the solution of **L1**, **L2**, and **L3**. The molar absorbance coefficient was measured and summarized in Table 2. The modulation of molar absorbance coefficient can be seen upon substitution of a new aromatic ring to ligand **L1**. The emission spectra of the ligand show emission maxima at around 433 nm (λ_{ex} at 290 nm, scan rate 200 and slit widths = 10 nm). As the concentration of the zinc ion in the **L1** solution rises, the emission intensity at 430 nm increases, which is related to the cancellation of the PET mechanism caused through the lone pair of the nitrogen donor (Figure S3). The solid state structure clarifies that ligand **L1** coordinates with the zinc ion in a 2:1 (**L1**/Zn^{2+}) ratio. Further, to determine the stoichiometry of complex formation in a solution state, measurements were performed through Job's plot method. A nonlinear fitting showed a maximum value at 0.66, which allows us to conclude that an alike solid state structure, in solution state stoichiometry complex remains the same 2:1 (**L1**/Zn^{2+}). Further, binding constant of complexation was calculated using the Benesi–Hildebrand method. The inverse of the concentration of zinc ion was plotted against the inverse of change in emission intensity. The slope and intercept of the curve were determined using a linear regression method, which allowed determining the binding constant equal to 1.4×10^5 M^{-1}. To check the working pH for binding studies, emission profiles were recorded at different pH values, suggesting that the receptor stabilizes at pH 4 to 9 pH. At basic pH, zinc hydroxide was formed and thus causing decomplexation and loss of fluorescence due to restoration of the PET channel. Therefore, all binding experiments were performed at pH 7.5.

The absorbance spectra of ligand **L2** has shown three absorbance maxima at 215, 245, and 295 nm (Figure S4), that correspond to the presence of two different chromophores in the system. Upon addition of zinc chloride, the absorbance intensity of the receptor (~215 nm) changes significantly. The emission spectra of ligand **L2** were taken in DMF/water (30:70) (λ_{ex} at 290 nm, scan rate 200 and slit widths = 10 nm). The emission spectrum of the complex has shown two peaks at 425 and 550 nm (Figure S5). As the concentration of zinc ion increases in a solution of complex **R2**, fluorescence intensity at 425 nm increases significantly, whereas little enhancement was observed at 550 nm. The loss of emission due to photo-induced electron transfer was inhibited through the coordination of the lone pair of benzimidazole with Zn(II). For **R1**, stoichiometry and binding constant of complex in solution state were calculated using Job's plot and Benesi–Hildebrand curve. The stoichiometry of complex found to be 1:1, which perfectly matches that of the solid state structure, and the binding constant was found to be 6.89×10^4 M^{-1}.

Binding Studies of Complexes R1 and R2 with Anionic Species. Due to the different electronic arrangement and orientation, three metal complexes offer an anion binding

DOI: 10.1021/acs.cgd.8b00165
Cryst. Growth Des. 2018, 18, 4320–4333

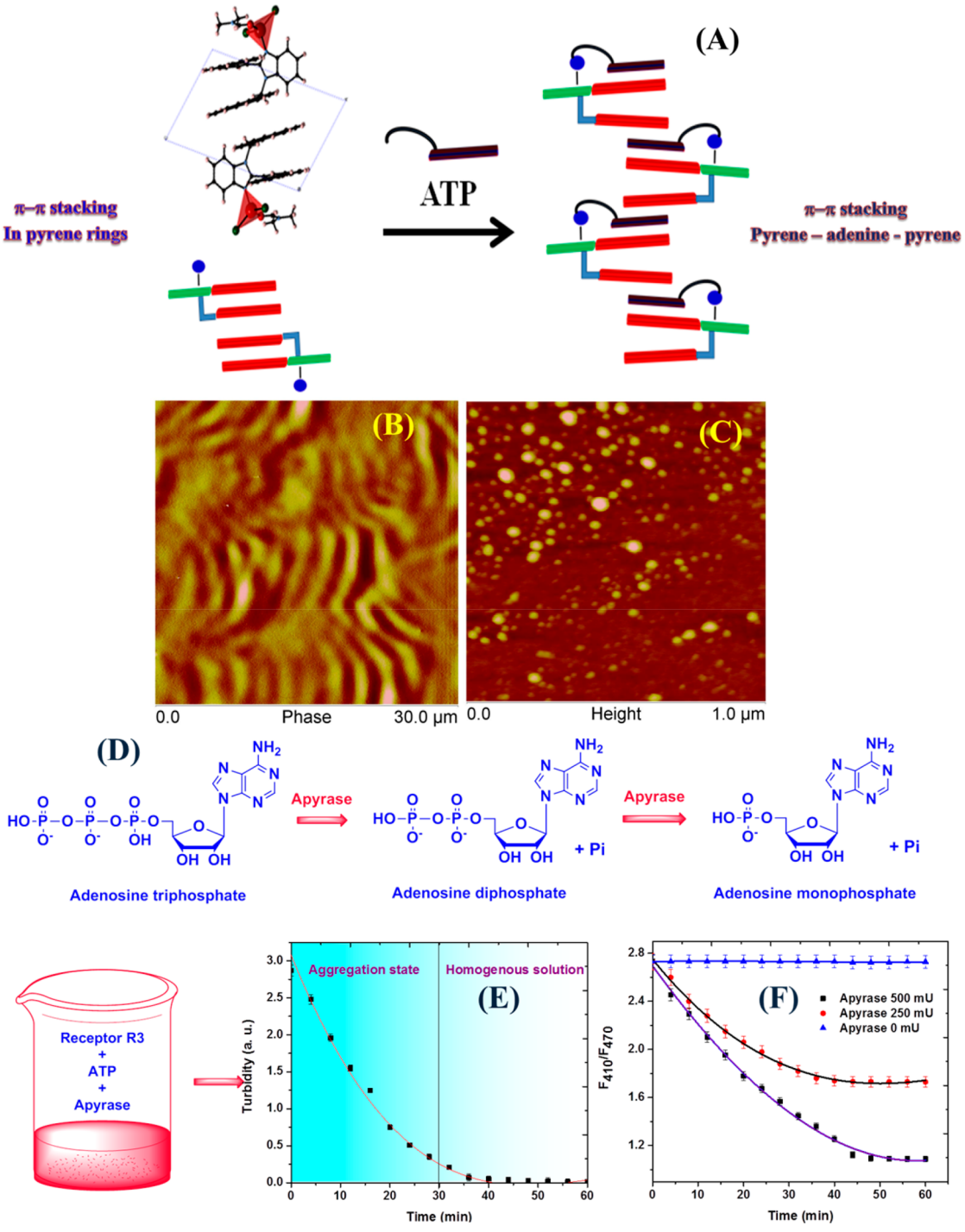

Figure 5. (A) Cartoon diagram of ATP induced gel formation. (B) AFM images of **R3** upon interaction with ATP in THF/water. (C) AFM images of **R3** upon interaction with ATP in DMF/water. (D) The reaction showing the hydrolysis of ATP in the presence of apyrase enzyme. (E) Change in turbidity of **R3** + ATP solution in DMF/water in the presence of apyrase with time. (F) Change in turbidity of **R3** + ATP solution in DMF/water in the presence of apyrase (0–250 mU) with time.

pattern, which is unique to the structure of receptor with anionic species. The fluorescence intensity of each complex was recorded in the presence of anions (F^-, Cl^-, Br^-, I^-, CH_3COO^-, NO_3^-, $H_2PO_4^-$, $P_2O_7^{4-}$, SO_4^{2-}) and ATP, AMP, and ADP. The complex **R1** showed enhancement in emission intensity upon interaction with ATP along with some interference with AMP and phosphate (Figures S6–S7). This enhancement in emission intensity is attributed to replacement of bromide with phosphate ion. The zinc ion has a tendency to bind strongly with a phosphate ion,[69,70] while the orientation of a complex also provides the selectivity for a particular analyte. Binding studies of complex **R2** was performed using fluorescence spectroscopy with various anionic species (Figure S8–S9). Similarly for the complex **R1**, the studies also show fluorescence enhancement with different phosphate species. As shown in Figure S10, ATP showed maximum fluorescence enhancement among investigated analysts. The stoichiometries of **R1** and **R2** complexes with ATP were evaluated using Job's

DOI: 10.1021/acs.cgd.8b00165
Cryst. Growth Des. 2018, 18, 4320–4333

plot, which indicates the formation of a 1:1 complex between **R2** and ATP. The major drawback of the **R2** sensor was its nonspecificity because it also shows emission enhancement with other phosphate ions (Figure S11). Therefore, it is not suitable for real time determination of ATP.

Photophysical Properties of Ligand L3 and Complex R3. The absorption and emission spectra of all complexes were recorded in DMF/H_2O, and the electronic absorption spectra of ligands and complexes are shown in Figure S12. Ligand **3** exhibited strong absorption bands at 248 nm, 277 nm, 330 and 345 nm (Figure S12). This is due to the presence of two pyrene subgroups in ligand **L3**, and four different absorption bands appeared. One pyrene ring is directly conjugated with the benzimidazole ring, whereas another ring is attached with benzimidazole through a methylene group. The conjugated pyrene group should absorb at a higher wavelength, and therefore peaks at 277 and 345 nm are due to $\pi-\pi^*$ and $n-\pi^*$ transitions of the conjugated pyrene ring. The peaks at 248 and 330 nm correspond, respectively, to $\pi-\pi^*$ and $n-\pi^*$ transitions of the pyrene ring attached with a methylene group. The emission spectra of ligand **L3**, taken in DMF/water (30:70) (λ_{ex} at 345 nm, scan rate 200 and slit widths = 10 nm), has shown four emission maxima at 380, 410, 440, and 470 nm. Here emission peaks at 410 and 470 nm correspond to the monomer and excimer state ($\pi-\pi$ stacking) of the receptor, respectively. It is interesting that, upon addition of the Zn(II) ion, the fluorescence intensity of the receptor increases significantly. This large enhancement in emission intensity has been rationalized by the cancellation of the photoinduced electron transfer mechanism. On complexation, the lone pair of benzimidazole ring causes the fluorescence quenching due to the PET phenomenon transferred to the zinc ion. However, the emission intensity at 470 nm enhanced due to the formation of excimers. To confirm the binding of Zn(II) with ligand **L3**, the titration was performed by successive addition of the zinc ion into 10 μM solution of complex **L3**. As shown in Figure 2a, the orientation of ligand **L3** changes on complexation with the zinc ion in such way that all the pyrene rings got stacked and gave a strong excimer emission band at 470 nm. The binding constant for **L3**−Zn(II) complex is calculated using the Benesi−Hildebrand method. A graph was plotted between the inverse of concentration of analyte and inverse of change in fluorescence (Figure S12). The binding constant has calculated from the intercept and slope of the curve, which was found to be 7.34×10^4.

Binding Studies of Complex R3 with Anionic Species. The binding behavior of complex **R3** was examined using fluorescence spectroscopy toward various anionic species such as iodide, bromide, chloride, fluoride, nitrate, dihydrogen phosphate, acetate, ATP, AMP, ADP, pyrophosphate (PPi), nicotinamide adenine dinucleotide (NADH), etc. Emission spectra of complex **R3** were recorded after the addition of 16 μM of each analyte (Figure 4), and it was observed that only ATP has shown a significant change in the emission profile of **R3**, whereas all other tested anionic species did not affect fluorescence profile of the complex. Interestingly, the emission at 410 nm (monomeric state) enhanced whereas emission due to the excimer state (470 nm) quenched as the concentration of ATP increases in the solution. This change in emission intensity can be explained on the basis of formation of a **R3**−**ATP** complex. Zinc ion coordinate with two bromide ions and one DMF molecule, which can be easily replaced by the phosphate ion of ATP. Upon replacement of two bromide ions, the fluorescence intensity at 410 nm increases; however, the **R3**−**ATP** complex alters the $\pi-\pi$ stacking interaction in such a way that luminescence due to the excimer state disappears. To analyze the binding behavior, emission spectra of **R3** were recorded by successive addition of ATP solution (0−16 μM). This allowed the ratiometric detection of ATP. The ratio of fluorescence intensity was plotted against the concentration of ATP added. The calibration plot for ATP exhibited a nonlinear regression up to 16 μM with an R^2 value of 0.9993 (Figure S13) and detection limit of 15 nM. To analyze the effect of another ion on detection of ATP, the competitive binding experiments were performed, which showed that none of the interfering ions obstruct the detection of ATP ion. Also, the UV−visible absorbance spectra of the **R3** complex were recorded with the addition of ATP in the THF/water (30:70) solvent system (Figure S15).

Binding Pattern of ATP with Receptor R3. To find out the stoichiometry of complexation, the Job's plot was constructed. The plot between mole fraction of ATP and [HG] shows a maximum value for [HG] at a mole fraction of 0.5, which indicates the 1:1 complexation between **R3** and ATP. The changes induced in excimer and the monomeric emission peak of the receptor **R3** indicate the breakdown of $\pi-\pi$ stacking (Figure 5); also the clear solution converts into a highly viscous liquid which formed a luminescent metallogel upon cooling. Earlier, Yoon et al. have studied the sandwich stacking of pyrene−adenine−pyrene for determination of ATP. Here adenine ring breaks the $\pi-\pi$ stacking in receptor and penetrate between two pyrene rings.[49] Similar results were obtained from fluorescence spectroscopy. Upon addition of ATP, two types of interactions were involved between receptor **R3** and ATP. One is ionic interaction and another is $\pi-\pi$ stacking between pyrene−adenine−pyrene sandwiches. In this way, the polymeric structure extended through hydrophobic $\pi-\pi$ stacking interaction was formed causing turbidity in the solution. The ratiometric change in emission (Figure S14) and increase in turbidity indicate that the clear solution changes into the aggregates. To find out the morphology of aggregates formed upon addition of ATP, atomic force microscopic images (AFM) of receptor **R3** were taken in the presence of ATP. AFM imaging confirmed the formation of aggregates (Figure 5B−C). Initially, the receptor **R3** was purely crystalline in nature. With the addition of 1.5 equiv of ATP, aggregates were formed as also confirmed using dynamic light scattering (DLS) experiments. The size of aggregates formed was determined using DLS, which showed the particles' size distribution in the range of 35−40 μm (Figure S16). To determine the stoichiometry of complex formation between ATP and complex **R3**, fluorescence data were utilized to construct Job's plots. The x-axis of the Job's plot is labeled as the mole fraction of ATP (Figure S17). The intersection of the two linear portions of the Job's plot gives the mole ratio corresponding to the binding stoichiometry between ATP and **R3**, which confirmed formation of the 1:1 complex between ATP and **R3**. The binding constant (K_a) of **R3** for ATP was also determined by constructing the Benesi−Hildebrand plot; a K_a value of 2.57 ($\pm$0.04) $\times 10^4$ M^{-1} was obtained from the slope and intercept of the line (Figure S18).

Gel Formation with the Interaction of ATP. All the binding studies were performed in water/DMF (70:30), while the solution of receptor **R3** turned turbid upon interaction with ATP. Further, we have examined the behavior of receptor **R3** with ATP in another solvent system. It was observed that in

DOI: 10.1021/acs.cgd.8b00165
Cryst. Growth Des. 2018, 18, 4320−4333

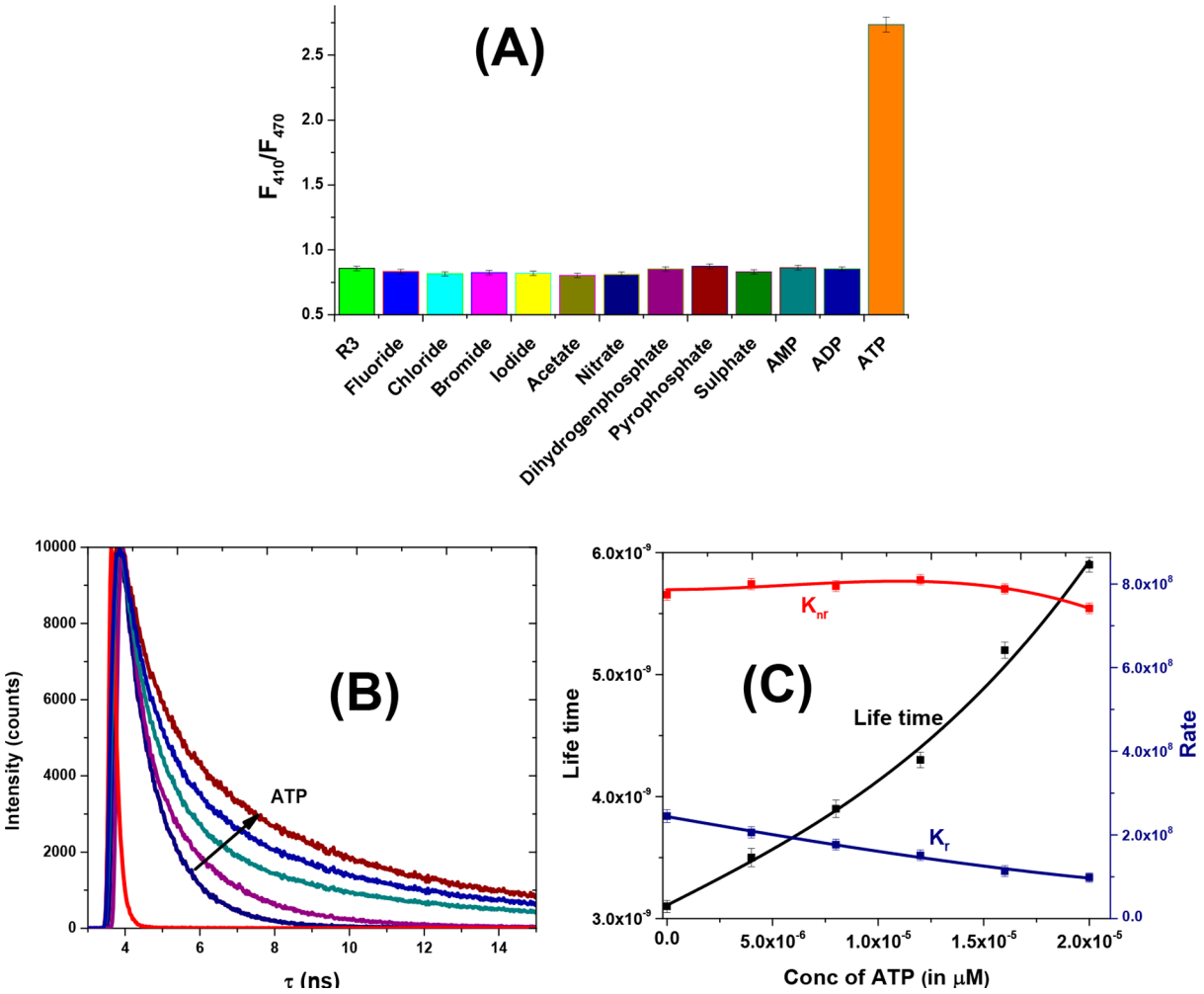

Figure 6. (A) Competing binding of complex **R3** with various anionic species. (B) Change in fluorescence lifetime of **R3** upon interaction with ATP. (C) The graph showing the variation of life time (left *Y*-axis) and decay constant (right *Y*-axis) of **R3** with increase in concentration of ATP.

tetrahydrofuran/water (30:70) the more viscous liquid was formed, which turned to metallogel upon cooling for 6 h. To investigate the morphology of gel, scanning tunneling microscopy images were recorded, and it was observed that a polymeric network was formed which quench the excimer fluorescence. As shown below in the cartoon diagram, ATP interacts with probe **R3** in such a way that the adenosine unit penetrates between two pyrene rings which abolished the $\pi-\pi$ interaction between two pyrene rings and induced a new sandwich complex having $\pi-\pi$ stacking between pyrene−adenosine−pyrene. Such planar conjugated systems are well-known for formation of a $\pi-\pi$ stacking induced gel.[71−73] This supramolecular assembly highly depends upon the anionic species, nature of interaction, and solvent system.[74−77] It is interesting that a metallogel is formed in THF/water (30:70), whereas aggregates are formed in DMF/water. Therefore, the gel formation is not only selective for anionic species (ATP) but also the solvent determines the morphology formed in the solution.

Selectivity of Receptor R3 for ATP. To investigate the interference caused by competing analytes, such as ADP, AMP, PPi, NADH and other anions, we recorded the corresponding fluorescence spectra. It was determined that ADP and AMP show a negligible change in monomeric and excimer emission peaks. Similarly, other analytes did not show any significant change in the emission profile. As shown in Figure 6, the ratio ($I_{monomer}/I_{excimer}$) for ATP is much larger as compared to other analytes. The above selectivity for ATP can be explained on the basis of the binding pattern. ATP binds with zinc ions through ionic bonds by replacing two bromide ions, and, similarly, AMP and ADP bind with receptor **R3** through ionic bonds. However, hydrophobic interaction ($\pi-\pi$ stacking) plays a crucial role in emission change. Therefore, due to the difference in chain length in ATP, AMP, and ADP, these analytes behave differently while interacting with receptor **R3**. For perfect binding or ratiometric sensing, it is necessary that both interactions (ionic and hydrophobic) occur simultaneously, which is possible only in the case of ATP. Thus, neither AMP nor ADP shows a response to receptor **R3** (Figure S19). Further, to validate the observation, the powder X-ray diffraction (XRD) spectra of complex **R3** were recorded and compared with the simulated XRD pattern, which were perfectly superimposed (Figure S24). Then the complex was reacted with ATP and ADP in THF/water, and after the solvent was removed with the vacuum, the prepared compound was washed with water, to remove the free phosphate species. The broad XRD pattern of **R3**−ATP revealed the formation of polymeric aggregates,[80] whereas solid state XRD spectra of **R3**-ADP showed sharp peaks, which also have similarity with XRD spectra of **R3** complex. To confirm

DOI: 10.1021/acs.cgd.8b00165
Cryst. Growth Des. 2018, 18, 4320−4333

the formation of the **R3**−ATP complex, Raman spectra were recorded. To record the Raman spectra, the crude obtained from the reaction of zinc complex**R3** with ATP was washed with distilled water to remove the unreacted adenosine triphosphate ions. The Raman spectra of this crude was expressively different from the pure **R3** complex and showed peaks corresponding to zinc−phosphate bonds and phosphorus−oxygen bonds (725 cm^{-1}, 1005 cm^{-1}, 1122 cm^{-1}), which confirm the formation of the **R3**−ATP complex (Figure S25). However, the ADP ion showed similar spectra as the complex **R3**, which reveals that complex **R3** is not reactive toward ADP. To confirm the complexation of ATP with complex **R3**, the chemical characterization of **R3** complex and **R3**−ATP was performed using energy-dispersive X-ray spectroscopy (Figure S26). It revealed that the complex **R3** has Zn, Br, C, N, and O; however, the bromide ion disappears upon complexation with ATP. The presence of the peak at 2.1 corresponds to phosphorus, which confirmed the replacement of the Br^- ion with the phosphate unit of ATP, whereas, in the crude of **R3**−ADP, the peak corresponding to Br still appears and a negligible presence of phosphorus was seen.

Biological Applications of Receptor R3. To analyze the response of the receptor to intercellular investigation of ATP, HeLa cells were investigated under a fluorescence microscope for an excitation wavelength of 340−380 nm and an emission wavelength of 435−485 nm for blue fluorescence. For the fluorescence microscopic experiments, HeLa cells were grown in Dulbecco's modified Eagle's medium (DMEM) using the reported protocol.[78] The cells were divided into two parts. Among these, one part was incubated with 10 μM of oligomycin that is well-known for its ATP syntheses inhibition activity. Then both parts were exposed to receptor **R3** (20 μM) for 3 h. Before the fluorescence measurement, the cells were washed with phosphate buffer solution (PBS). The receptor **R3** caused a loss in fluorescence in the oligomycin part, whereas the HeLa cells incubated with only probe **R3** show emission (Figure S20). These experiments showed that receptor **R3** is capable to determine ATP in the presence of another inorganic phosphate such as AMP and ADP in the intercellular system. Further, the ratiometric emission conversion with ATP was used to explore the probe **R3** to study the activity of the apyrase enzyme that is well-known for hydrolysis of nucleotide triphosphates. Our probe **R3** shows a ratiometric response only with ATP, and therefore upon hydrolysis the signature emission profile of the **R3**−ATP complex should disappear. With this in mind, a solution of **R3** (20 μM), ATP (20 μM), and apyrase was prepared at pH 6, and an emission profile was recorded after a short interval of time. The curve (Figure 5) shows that in the absence of apyrase, fluorescence intensity ($F_{410\ nm}/F_{470\ nm}$) remains almost unchanged; however, in the presence of two different concentrations of apyrase it decreases dramatically, which validates the conversion of ATP into AMP and ADP and finally into phosphates. To explore the mechanism more deeply, the turbidity of the solution was measured with time, which also shows a continuous decrease with time (up to 60 min) (Figure 5). Thus, the prepared probe can be used for monitoring the activity of the apyrase enzyme.

Fluorescence Decay Time and Radiative Constant. Fluorescence is a perfect nanoscale probe as its decay could take place on the nanosecond level. Therefore, it is a promising technique to evaluate molecular interactions and changes in a nanoenvironment. To analyze the effect of aggregation on photophysical properties and decay time, time-resolved fluorescence spectra were recorded at the wavelength of 472 nm, which enlightens the mechanism of sensing of ATP. Fluorescence quantum yield and lifetime were determined using time-resolved fluorescence and radiative decay constant using the following formulas:

$$^{\Phi}f = \frac{K_r}{K_r + K_{nr}} \quad \text{and} \quad \tau = \frac{1}{K_r + K_{nr}}$$

where $^{\Phi}_{f}$ is fluorescence quantum yield, τ is a lifetime, K_r is radiative decay constant, and K_{nr} is nonradiative decay constant.

The rate of radiative decay of the excited state decreases as the concentration of ATP increases in solution, whereas the lifetime of the excited state increases. This transformation is due to the formation of aggregates where properties of the excited state are different and lead to an increased lifetime,[79] whereas a decreasing radiative decay constant is attributed to quenching of the excimer emission. We observed a minor change in the nonradiative decay constant upon addition of ATP to the **R3** solution.

CONCLUSION

In summary, we have synthesized three zinc complexes tagged with fluorescence moieties that can form a tertiary complex with biologically important phosphates. Upon addition of ATP, the complex **R1** showed distinct spectroscopic behavior due to the replacement of the bromide ion. **R1** and **R2** interact only through ionic interaction with phosphates. Therefore, these complexes show emission enhancements with ATP along with some interference of AMP and phosphate. The complex **R3** has a tendency to interact through by both $\pi-\pi$ stacking and ionic interaction. It selectively binds with ATP even in the presence of other phosphates. Two types of interactions act differently on emission properties of the complex. Ionic interactions cause enhancement in fluorescence intensity at 410 nm, whereas the $\pi-\pi$ stacking interaction between pyrene and adenosine ring quenches the emission at 470 nm. Thus, the pyrene conjugated complex of zinc (**R3**) is capable of detecting ATP ratiometrically with a low detection limit. Furthermore, complex **R3** was explored for monitoring the activity of apyrase enzyme during hydrolysis of ATP. The outcome of this work is important for the development of a highly selective ATP sensor using ionic and other noncovalent interactions.

EXPERIMENTAL SECTION

General Information. *ortho*-Phenylenediamine, aldehydes, and biomolecules (Analytical grade) were procured from Sigma-Aldrich and used without further purification. Oligomycin (from Streptomyces diastatochromogenes) and apyrase enzyme (From Potato) were purchased from Sigma-Aldrich. Methanol and tetrahydrofuran were purchased from Merck. The photoluminescence experiments were performed on a PerkinElmer LS-55 instrument at a constant scan speed of 200. For all experiments, excitation and emission slit widths were kept at 10 nm. ^{1}H NMR and the ^{13}C NMR spectrum were recorded on a Jeol instrument, which was operated at 400 MHz for ^{1}H NMR and 100 MHz for ^{13}C NMR. Single crystal data for three complexes were measured on Bruker X8 APEXIII KAPPA CCD diffractometer at room temperature using graphite monochromatized Mo−Kα radiation (λ = 0.71073 Å). Elemental analyses were carried out using Fisons CHNS analyzers. The morphology of gel was determined on a scanning electron microscope (SEM JEOL JSM-6610LV) using a voltage of 15 kV and atomic force microscopy

DOI: 10.1021/acs.cgd.8b00165
Cryst. Growth Des. 2018, 18, 4320−4333

(AFM). The particle size of nanoparticles was determined by dynamic light scattering (DLS) using the external probe feature of Metrohm Microtrac Ultra Nanotrac particle size analyzers. Fluorescence microscopy of HeLa cells was recorded on a Leica fluorescence microscope. Fluorescence lifetime was calculated from time-resolved fluorescence spectroscopy using a PicoQuant fluorescence spectrophotometer.

Detail of UV−visible Absorbance and Fluorescence Measurements. The stock solution of each ligand (10 μM) was prepared in DMF/water (30:70). Similarly, a stock solution of zinc bromide and zinc chloride (each 1 mM) was prepared in hot distilled water and diluted further as a requirement of the experiment. The solution of various anions as tetra butyl ammonium salt (F^-, Cl^-, Br^-, I^-, CH_3COO^-, NO_3^-, $H_2PO_4^-$, $P_2O_7^{4-}$, SO_4^{2-}) (1 mM) and ATP (adenosine triphosphate), AMP (adenosine monophosphate), and ADP (adenosine diphosphate) (1 mM) were prepared in distilled water. The pH of the solution was maintained at 7.0 using 1 mM HEPES buffer solution.

Synthesis of L1 (1-Benzyl-2-phenyl-1*H*-benzo[d]-imidazole).[51] In a round-bottom flask, the benzaldehyde (2.44 g, 10 mmol) and *o*-phenylenediamine (1.08 g, 10 mmol) was dissolved in 50 mL of methanol along with (0.185 g, 0.5 mmol) of zinc perchlorate. The reaction mixture was refluxed for 8 h, and the progress of the reaction was monitor using TLC. After completion of the reaction, the mixture was allowed to cool to room temperature. The orange crystalline solid was separated out, which constituted pure compound **L1** with the following properties. Yield 94%. Elemental analysis: Calculated: C, 84.48; H, 5.67; N, 9.85; Found: C, 84.42; H, 5.61; N, 9.78.

Synthesis of L2 (2-(Naphthalene-1-yl)-1-(naphthalene-1-ylmethyl)-1*H*-benzo[d]imidazole). The compound **L2** was synthesized using the same method as **L1**, naphthaldehyde (3.44 g, 10 mmol) was used instead of benzaldehyde, and reaction mixture was refluxed for 10 h. The orange solid was separated out after 10 h of refluxing, which constituted pure compound **L2** with the following properties. Yield 91%. Elemental analysis: Calculated: C, 87.47; H, 5.24; N, 7.29; Found: C, 87.41; H, 5.17; N, 9.27.

Synthesis of L3 (1-((4,5a1-dihydropyren-1-yl)methyl)-2-(pyren-1-yl)-1*H*-benzo[d]imidazole). The compound **L3** was synthesized using same method as **L1**, 1-pyrenecarboxaldehyde (4.96 g, 10 mmol) was used instead of benzaldehyde and reaction mixture was refluxed for 10 h. The orange solid was separated out after 10 h of refluxing, which constituted pure compound **L3** with following properties. Yield 91%. Elemental analysis: Calculated: C, 89.86; H, 4.90; N, 5.24; Found: C, 89.82; H, 4.85; N, 5.18. ^{1}H NMR (400 MHz, DMSO-d_6) δ 8.01−7.94 (t, 4H, J = 8 Hz), 7.86−7.79 (t, 4H, J = 8 Hz), 7.69 (t, 1H, J = 8 Hz), 7.61 (t, 2H, J = 8 Hz), 7.57 (t, 2H, J = 8 Hz), 7.51 (t, 2H, J = 8 Hz), 7.45 (t, 3H, J = 8 Hz), 7.38 (t, 2H, J = 8 Hz), 7.28 (t, 1H, J = 8 Hz), 7.22 (t, 3H, J = 8 Hz), 6.60 (d, 1H, J = 8 Hz), 5.83 (s, 2H).^{13}C NMR (400 MHz, DMSO-d_6) δ 175.70, 152.80, 151.86, 144.40, 143.35, 135.87, 134.94, 134.13, 133.71, 133.59, 132.46, 132.04, 131.00, 130.69, 130.29, 129.11, 128.92, 128.85, 128.73, 128.39, 128.27, 127.84, 127.61, 126.99, 126.94, 126.87, 126.59, 125.91, 125.83, 125.53, 123.63, 123.38, 123.19, 122.79, 122.13, 120.03, 119.60, 111.88, 111.79, 46.12.

Synthesis of Complex R1. Zinc(II) bromide (100 mmol) was dissolved in methanol−tetrahydrofuran (20 mL) along with ligand **L1** (200 mmol). The reaction mixture was heated and stirred for 20 min. The color of the solution becomes more intense. The solution was kept undisturbed for 24 h for slow evaporation. Dark brown, needle shaped crystals were formed that were suitable for single crystal data collection. Elemental analysis: Calculated: C, 60.52; H, 4.06; N, 7.06; Found: C, 60.47; H, 4.00; N, 7.01.

Synthesis of Complex R2. Zinc(II) chloride (100 mmol) was dissolved in methanol−tetrahydrofuran (20 mL) along with ligand **L1** (200 mmol) The reaction mixture was heated and stirred for 20 min. The color of the solution becomes more intense. The solution was kept undisturbed for 24 h for slow evaporation. Dark brown, needle shaped crystals were formed that were suitable for single crystal data collection. Elemental analysis: Calculated: C, 62.70; H, 4.58; N, 7.08; Found: C, 62.67; H, 4.55; N, 7.02.

Synthesis of Complex R3. Zinc(II) bromide (100 mmol) was dissolved in methanol−tetrahydrofuran (20 mL) along with ligand **L1** (200 mmol). The reaction mixture was heated and stirred for 20 min. The color of the solution becomes more intense. The solution was kept undisturbed for 24 h for slow evaporation. Dark brown, needle-shaped crystals were formed that were suitable for single crystal data collection. Elemental analysis: Calculated: C, 62.01; H, 3.99; N, 5.04; Found: C, 61.95; H, 3.95; N, 5.00.

■ ASSOCIATED CONTENT

Supporting Information

The Supporting Information is available free of charge on the ACS Publications website at DOI: 10.1021/acs.cgd.8b00165.

Absorption and emission properties, ^{1}H NMR, ^{13}C NMR, bond angles and bond length of complex, DLS, fluorescence microscopy images (PDF)

Accession Codes

CCDC 1526966−1526968 contain the supplementary crystallographic data for this paper. These data can be obtained free of charge via www.ccdc.cam.ac.uk/data_request/cif, or by emailing data_request@ccdc.cam.ac.uk, or by contacting The Cambridge Crystallographic Data Centre, 12 Union Road, Cambridge CB2 1EZ, UK; fax: +44 1223 336033.

■ AUTHOR INFORMATION

Corresponding Author

*E-mail: nsingh@iitrpr.ac.in. Tel: +91-1881242176.

ORCID

Amanpreet Singh: 0000-0002-1461-4607
Jan J. Dubowski: 0000-0003-0022-527X
Narinder Singh: 0000-0002-8794-8157

Notes

The authors declare no competing financial interest.

■ ACKNOWLEDGMENTS

This work was supported by a research grant from Indo-Canada Project sponsored by DBT-New Delhi and IC-IMPACTS Canada. A.S. and P.R. are thankful to CSIR-New Delhi (9/1005(0010)/2014-EMR-1) and UGC-New Delhi respectively for their fellowships.

■ REFERENCES

(1) Gale, P. A.; Caltagirone, C. Anion Sensing by Small Molecules and Molecular Ensembles. *Chem. Soc. Rev.* **2015**, *44* (13), 4212−4227.

(2) Gong, Z.-L.; Zhong, Y.-W. $H_2PO_4^-$ - and Solvent-Induced Polymorphism of an Amide-Functionalized [Pt(N^C^N)Cl] Complex. *Inorg. Chem.* **2016**, *55* (20), 10143−10151.

(3) Patra, C.; Bhanja, A. K.; Mahapatra, A.; Mishra, S.; Saha, K. D.; Sinha, C. Coumarinyl Thioether Schiff Base as a Turn-on Fluorescent Zn(II) Sensor and the Complex as Chemosensor for the Selective Recognition of ATP, along with Its Application in Whole Cell Imaging. *RSC Adv.* **2016**, *6* (80), 76505−76513.

(4) Raj, P.; Singh, A.; Kaur, K.; Aree, T.; Singh, A.; Singh, N. Fluorescent Chemosensors for Selective and Sensitive Detection of Phosmet/Chlorpyrifos with Octahedral Ni^{2+} Complexes. *Inorg. Chem.* **2016**, *55*, 4874−4883.

(5) Singh, A.; Singh, A.; Singh, N.; Jang, D. O. A 2-Mercaptobenzimidazole-Based Emissive Cu(I) Complex for Selective Determination of Iodide with Large Stokes Shift. *Sens. Actuators, B* **2017**, *243*, 372−379.

DOI: 10.1021/acs.cgd.8b00165
Cryst. Growth Des. 2018, 18, 4320−4333

(6) Lu, Q.-S.; Dong, L.; Zhang, J.; Li, J.; Jiang, L.; Huang, Y.; Qin, S.; Hu, C.-W.; Yu, X.-Q. Imidazolium-Functionalized BINOL as a Multifunctional Receptor for Chromogenic and Chiral Anion Recognition. *Org. Lett.* **2009**, *11* (3), 669−672.
(7) Fu, Y.; Mu, L.; Zeng, X.; Zhao, J.-L.; Redshaw, C.; Ni, X.-L.; Yamato, T. An NBD-Armed thiacalix[4]arene-Derived Colorimetric and Fluorometric Chemosensor for Ag^{+}: A Metal-Ligand Receptor of Anions. *Dalton Trans.* **2013**, *42* (10), 3552−3560.
(8) Kundu, T.; Chowdhury, A. D.; De, D.; Mobin, S. M.; Puranik, V. G.; Datta, A.; Lahiri, G. K. Selective Recognition of Fluoride and Acetate by a Newly Designed Ruthenium Framework: Experimental and Theoretical Investigations. *Dalt. Trans.* **2012**, *41* (15), 4484.
(9) Singh, A.; Raj, P.; Singh, N. Benzimidazolium-Based Self-Assembled Fluorescent Aggregates for Sensing and Catalytic Degradation of Diethylchlorophosphate. *ACS Appl. Mater. Interfaces* **2016**, *8*, 28641−28651.
(10) Yang, Y.; Chen, S.; Ni, X. Fluorescent Chemosensor for Nitrate in Acidic Aqueous Solution and. *Anal. Chem.* **2015**, *87* (14), 7461−7466.
(11) Zhao, J.; Yang, D.; Zhao, Y.; Cao, L.; Zhang, Z.; Yang, X.-J.; Wu, B. Phosphate-Induced Fluorescence of a Tetraphenylethene-Substituted Tripodal Tris(urea) Receptor. *Dalt. Trans.* **2016**, *45* (17), 7360−7365.
(12) Jia, C.; Zuo, W.; Zhang, D.; Yang, X.; Wu, B. Anion Recognition by Oligo-(Thio)urea-Based Receptors. *Chem. Commun.* **2016**, *52*, 9614−9627.
(13) Singh, J.; Singh, A.; Singh, N. Urea Based Organic Nanoparticles for Selective Determination of NADH. *RSC Adv.* **2014**, *4* (106), 61841−61846.
(14) Singh, A.; Singh, A.; Singh, N.; Jang, D. O. A Benzimidazolium-Based Organic Trication: A Selective Fluorescent Sensor for Detecting Cysteine in Water. *RSC Adv.* **2015**, *5* (88), 72084−72089.
(15) Wang, S.; Chang, Y.-T. Combinatorial Synthesis of Benzimidazolium Dyes and Its Diversity Directed Application toward GTP-Selective Fluorescent Chemosensors. *J. Am. Chem. Soc.* **2006**, *128* (32), 10380−10381.
(16) Hargrove, A. E.; Nieto, S.; Zhang, T.; Sessler, J. L.; Anslyn, E. V. Artificial Receptors for the Recognition of Phosphorylated Molecules. *Chem. Rev.* **2011**, *111*, 6603−6782.
(17) Rommel, S. A.; Sorsche, D.; Rau, S. A Supramolecular H-Bond Driven Light Switch Sensor for Small Anions. *Dalt. Trans.* **2016**, *45* (1), 74−77.
(18) Singh, A.; Singh, A.; Singh, N.; Jang, D. O. Selective Detection of Hg (II) with Benzothiazole-Based Fl Uorescent Organic Cation and the Resultant Complex as a Ratiometric Sensor for Bromide in Water. *Tetrahedron* **2016**, *72* (24), 3535−3541.
(19) Kumar, S.; Singh, P.; Mahajan, A.; Kumar, S. Aggregation Induced Emission Enhancement in Ionic Self-Assembled Aggregates of Benzimidazolium Based Cyclophane and Sodium Dodecylbenzenesulfonate. *Org. Lett.* **2013**, *15* (13), 3400−3403.
(20) Yao, J.; Fu, Y.; Xu, W.; Fan, T.; Gao, Y.; He, Q.; Zhu, D.; Cao, H.; Cheng, J. Concise and Efficient Fluorescent Probe via an Intromolecular Charge Transfer for the Chemical Warfare Agent Mimic Diethylchlorophosphate Vapor Detection. *Anal. Chem.* **2016**, *88* (4), 2497−2501.
(21) Liu, X.; Xu, J.; Lv, Y.; Wu, W.; Liu, W.; Tang, Y. An ATP-Selective, Lanthanide Complex Luminescent Probe. *Dalton Trans.* **2013**, *42* (27), 9840−9846.
(22) Kumar, A.; Pandey, R.; Kumar, A.; Gupta, R. K.; Dubey, M.; Mohammed, A.; Mobin, S. M.; Pandey, D. S. Self-Assembled copper(II) Metallacycles Derived from Asymmetric Schiff Base Ligands: Efficient Hosts for ADP/ATP in Phosphate Buffer. *Dalt. Trans.* **2015**, *44*, 17152−17165.
(23) Minami, T.; Emami, F.; Nishiyabu, R.; Kubo, Y.; Anzenbacher, P. Quantitative Analysis of Modeled ATP Hydrolysis in Water by a Colorimetric Sensor Array. *Chem. Commun.* **2016**, *52* (10), 7838−7841.
(24) Vancraenenbroeck, R.; Webb, M. R. A Fluorescent, Reagentless Biosensor for ATP, Based on Malonyl-Coenzyme A Synthetase. *ACS Chem. Biol.* **2015**, *10* (11), 2650−2657.
(25) Liu, Z.; Chen, S.; Liu, B.; Wu, J.; Zhou, Y.; He, L.; Ding, J.; Liu, J. Intracellular Detection of ATP Using an Aptamer Beacon Covalently Linked to Graphene Oxide Resisting Non- Specific Probe Displacement. *Anal. Chem.* **2014**, *86*, 12229−12235.
(26) Asha, K. S.; Bhattacharyya, K.; Mandal, S. Discriminative Detection of Nitro Aromatic Explosives by a Luminescent Metal−organic Framework. *J. Mater. Chem. C* **2014**, *2* (47), 10073−10081.
(27) Au, V. K. M.; Zhu, N.; Yam, V. W. W. Luminescent Metallogels of Bis-Cyclometalated alkynylgold(III) Complexes. *Inorg. Chem.* **2013**, *52* (2), 558−567.
(28) Ghosh, S.; Mishra, M. K.; Ganguly, S.; Desiraju, G. R. Dual Stress and Thermally Driven Mechanical Properties of the Same Organic Crystal: 2,6-Dichlorobenzylidene-4-Fluoro-3-Nitroaniline. *J. Am. Chem. Soc.* **2015**, *137* (31), 9912−9921.
(29) Banik, M.; Gopi, S. P.; Ganguly, S.; Desiraju, G. R. Cocrystal and Salt Forms of Furosemide: Solubility and Diffusion Variations. *Cryst. Growth Des.* **2016**, *16*, 5418−5428.
(30) Rana, L. K.; Sharma, S.; Hundal, G. First Report on Crystal Engineering of Hg(II) Halides with Fully Substituted 3,4-Pyridinedicarboxamides: Generation of Two-Dimensional Coordination Polymers and Linear Zig-Zag Chains of Mercury Metal Ions. *Cryst. Growth Des.* **2016**, *16* (1), 92−107.
(31) Jassal, A. K.; Sharma, S.; Hundal, G.; Hundal, M. S. Structural Diversity, Thermal Studies, and Luminescent Properties of Metal Complexes of Dinitrobenzoates: A Single Crystal to Single Crystal Transformation from Dimeric to Polymeric Complex of copper(II). *Cryst. Growth Des.* **2015**, *15* (1), 79−93.
(32) Chung, C. Y. S.; Li, S. P. Y.; Lo, K. K. W.; Yam, V. W. W. Synthesis and Electrochemical, Photophysical, and Self-Assembly Studies on Water-Soluble pH-Responsive Alkynylplatinum(II) Terpyridine Complexes. *Inorg. Chem.* **2016**, *55* (9), 4650−4663.
(33) Ghosh, S.; Mukherjee, P. S. Self-Assembly of a Nanoscopic Prism via an Organometallic Pt 3 Acceptor and Its Fluorescent Detection of Nitroaromatics. *Organometallics* **2008**, *27*, 316−319.
(34) Ghosh, S.; Mukherjee, P. S. Self-Assembly of Molecular Nanoball: Design, Synthesis, and Characterization. *J. Org. Chem.* **2006**, *71* (22), 8412−8416.
(35) Lee, J. H. Y. H. Y.; Kang, S.; Lee, J. H. Y. H. Y.; Jung, J. H. A Tetrazole-Based Metallogel Induced with Ag^{+} Ion and Its Silver Nanoparticle in Catalysis. *Soft Matter* **2012**, *8*, 6557−6563.
(36) Aiyappa, H. B.; Saha, S.; Wadge, P.; Banerjee, R.; Kurungot, S. Fe(III) Phytate Metallogel as a Prototype Anhydrous, Intermediate Temperature Proton Conductor. *Chem. Sci.* **2015**, *6* (1), 603−607.
(37) Tam, A. Y.-Y.; Yam, V. W.-W. Recent Advances in Metallogels. *Chem. Soc. Rev.* **2013**, *42* (4), 1540−1567.
(38) Feldner, T.; Haring, M.; Saha, S.; Esquena, J.; Banerjee, R.; Diaz, D. D. Supramolecular Metallogel That Imparts Self-Healing Properties to Other Gel Networks. *Chem. Mater.* **2016**, *28* (9), 3210−3217.
(39) Sarmah, K.; Pandit, G.; Das, A. B.; Sarma, B.; Pratihar, S. Steric Environment Triggered Self-Healing CuII/HgII Bimetallic Gel with Old CuII−Schiff Base Complex as a New Metalloligand. *Cryst. Growth Des.* **2017**, *17*, 368−380.
(40) Maity, D.; Kumar, V.; Govindaraju, T. Reactive Probes for Ratiometric Detection of Co^{2+} and Cu^{+} Based on ESIPT Mechanism. *Org. Lett.* **2012**, *14*, 6008−6011.
(41) Nishizawa, S.; Kato, Y.; Teramae, N. Fluorescence Sensing of Anions via Intramolecular Excimer Formation in a Pyrophosphate-Induced Self-Assembly of a Pyrene-Functionalized Guanidinium Receptor [9]. *J. Am. Chem. Soc.* **1999**, *121* (40), 9463−9464.
(42) Chen, S.; Shi, Z.; Qin, L.; Jia, H.; Zheng, H. Two New Luminescent Cd(II)-Metal−Organic Frameworks as Bifunctional Chemosensors for Detection of Cations Fe^{3+}, Anions CrO_4^{2-}, and $Cr_2O_7^{2-}$ in Aqueous Solution. *Cryst. Growth Des.* **2017**, *17*, 67−72.

DOI: 10.1021/acs.cgd.8b00165
Cryst. Growth Des. 2018, 18, 4320−4333

(43) Wang, D.; Li, S.-M.; Zheng, J.-Q.; Kong, D.-Y.; Zheng, X.-J.; Fang, D.-C.; Jin, L.-P. Coordination-Directed Stacking and Aggregation-Induced Emission Enhancement of the Zn(II) Schiff Base Complex. *Inorg. Chem.* **2017**, *56*, 984−990.
(44) Wang, D.; Li, S.-M.; Li, Y.-F.; Zheng, X.-J.; Jin, L.-P. Hydrogen Bond-Assisted Aggregation-Induced Emission and Application in the Detection of the Zn(II) Ion. *Dalton Trans.* **2016**, *45*, 8316−8319.
(45) Haldar, R.; Prasad, K.; Samanta, P. K.; Pati, S.; Maji, T. K. Luminescent Metal-Organic Complexes of Pyrene or Anthracene Chromophores: Energy Transfer Assisted Amplified Exciplex Emission and Al^{3+} Sensing. *Cryst. Growth Des.* **2016**, *16* (1), 82−91.
(46) Manalo, M. N.; Perez, L. M.; LiWang, A. Hydrogen-Bond & π-π Base-Stacking Interactions Are Coupled in DNA, As Suggested by Calcd & Exptl Trans-H Bond 2H Isotope Shifts. *J. Am. Chem. Soc.* **2007**, *129* (37), 11298−11299.
(47) Copeland, K. L.; Pellock, S. J.; Cox, J. R.; Cafiero, M. L.; Tschumper, G. S. Examination of Tyrosine/adenine Stacking Interactions in Protein Complexes. *J. Phys. Chem. B* **2013**, *117* (45), 14001−14008.
(48) Kumar Verma, R.; Takei, F.; Nakatani, K. Synthesis and Photophysical Properties of Fluorescence Molecular Probe for Turn-ON-Type Detection of Cytosine Bulge DNA. *Org. Lett.* **2016**, *18* (13), 3170−3173.
(49) Xu, Z.; Singh, N. J.; Lim, J.; Pan, J.; Ha, N. K.; Park, S.; Kim, K. S.; Yoon, J. Unique Sandwich Stacking of Pyrene-Adenine-Pyrene for Selective and Ratiometric Fluorescent Sensing of ATP at Physiological pH. *J. Am. Chem. Soc.* **2009**, *131*, 15528−15533.
(50) Kataev, E.; Arnold, R.; Ruffer, T.; Lang, H. Fluorescence Detection of Adenosine Triphosphate in an Aqueous Solution Using a Combination of Copper(II) Complexes. *Inorg. Chem.* **2012**, *51* (Ii), 7948−7950.
(51) Sharma, H.; Kaur, N.; Singh, N.; Jang, D. O. Synergetic Catalytic Effect of Ionic Liquids and ZnO Nanoparticles on the Selective Synthesis of 1,2-Disubstituted Benzimidazoles Using a Ball-Milling Technique. *Green Chem.* **2015**, *17* (8), 4263−4270.
(52) Bourhis, L. J.; Dolomanov, O. V.; Gildea, R. J.; Howard, J. A. K.; Puschmann, H. The Anatomy of a Comprehensive Constrained, Restrained Refinement Program for the Modern Computing Environment - Olex2 Dissected. *Acta Crystallogr., Sect. A: Found. Adv.* **2015**, *71* (1), 59−75.
(53) Morita, Y.; Suzuki, S.; Sato, K.; Takui, T. Synthetic Organic Spin Chemistry for Structurally Well-Defined Open-Shell Graphene Fragments. *Nat. Chem.* **2011**, *3* (3), 197−204.
(54) Chi, Y.-H.; Yu, L.; Shi, J.-M.; Zhang, Y.-Q.; Hu, T.-Q.; Zhang, G.-Q.; Shi, W.; Cheng, P. π-π Stacking and Ferromagnetic Coupling Mechanism on a Binuclear Cu(II) Complex. *Dalt. Trans.* **2011**, *40*, 1453−1462.
(55) Mobin, S. M.; Srivastava, A. K.; Mathur, P.; Lahiri, G. K. Vapor-Diffusion-Mediated Single Crystal-to-Single Crystal Transformation of a Discrete Dimeric copper(II) Complex to a Discrete Tetrameric copper(II) Complex. *Inorg. Chem.* **2009**, *48* (11), 4652−4654.
(56) Mobin, S. M.; Srivastava, A. K.; Mathur, P.; Lahiri, G. K. Single-Crystal to Single-Crystal Transformations in Discrete Hydrated Dimeric Copper Complexes. *Dalton Trans.* **2010**, *39* (6), 1447−1449.
(57) Vij, V.; Tiwari, J. N.; Kim, K. S. Covalent versus Charge Transfer Modification of Graphene/Carbon-Nanotubes with Vitamin B1: Co/N/S-C Catalyst toward Excellent Oxygen Reduction. *ACS Appl. Mater. Interfaces* **2016**, *8* (25), 16045−16052.
(58) Georgakilas, V.; Tiwari, J. N.; Kemp, K. C.; Perman, J. A.; Bourlinos, A. B.; Kim, K. S.; Zboril, R. Noncovalent Functionalization of Graphene and Graphene Oxide for Energy Materials, Biosensing, Catalytic, and Biomedical Applications. *Chem. Rev.* **2016**, *116* (9), 5464−5519.
(59) Sivaraman, G.; Anand, T.; Chellappa, D. Development of a Pyrene Based "turn On" Fluorescent Chemosensor for Hg^{2+}. *RSC Adv.* **2012**, *2* (28), 10605.
(60) Vidya, B.; Iniya, M.; Sivaraman, G.; Sumesh, R. V.; chellappa, D. Diverse Benzothiazole Based Chemodosimeters for the Detection of Cyanide in Aqueous Media and in HeLa Cells. *Sens. Actuators, B* **2017**, *242*, 434−442.
(61) Sivaraman, G.; Anand, T.; Chellappa, D. Pyrene Based Selective-Ratiometric Fluorescent Sensing of Zinc and Pyrophosphate Ions. *Anal. Methods* **2014**, *6* (7), 2343−2348.
(62) Mandal, S.; Kundi, V.; Seth, D. K.; Srikanth, K.; Gupta, P. Studies on Ruthenium Complexes of Pyrene-Appended Schiff Base Ligands. *Polyhedron* **2014**, *80*, 290−297.
(63) Gonell, S.; Peris, E. Pyrene-Based Mono- and Di-N-Heterocyclic Carbene Ligand Complexes of Ruthenium for the Preparation of Mixed Arylated/alkylated Arylpyridines. *ACS Catal.* **2014**, *4* (8), 2811−2817.
(64) Maity, D.; Bhaumik, C.; Mondal, D.; Baitalik, S. Ru(II) and Os(II) Complexes Based on Terpyridyl-Imidazole Ligand Rigidly Linked to Pyrene: Synthesis, Structure, Photophysics, Electrochemistry, and Anion-Sensing Studies. *Inorg. Chem.* **2013**, *52* (24), 13941−13955.
(65) Chong, Y. S.; Dial, B. E.; Burns, W. G.; Shimizu, K. D. Covalent Locking and Unlocking of an Atropisomeric Molecular Switch. *Chem. Commun.* **2012**, *48* (9), 1296−1298.
(66) Dial, B. E.; Pellechia, P. J.; Smith, M. D.; Shimizu, K. D. Proton Grease: An Acid Accelerated Molecular Rotor. *J. Am. Chem. Soc.* **2012**, *134* (8), 3675−3678.
(67) Liang, L. J.; Zhao, X. J.; Huang, C. Z. Zn(II) Complex of Terpyridine for the Highly Selective Fluorescent Recognition of Pyrophosphate. *Analyst* **2012**, *137* (4), 953−958.
(68) Isaia, F.; Aragoni, M. C.; Arca, M.; Bettoschi, A.; Caltagirone, C.; Castellano, C.; Demartin, F.; Lippolis, V.; Pivetta, T.; Valletta, E. Zinc(ii)-Methimazole Complexes: Synthesis and Reactivity. *Dalt. Trans.* **2015**, *44* (21), 9805−9814.
(69) Mesquita, L. M.; André, V.; Esteves, C. V.; Palmeira, T.; Berberan-Santos, M. N.; Mateus, P.; Delgado, R. Dinuclear Zinc(II) Macrocyclic Complex as Receptor for Selective Fluorescence Sensing of Pyrophosphate. *Inorg. Chem.* **2016**, *55* (5), 2212−2219.
(70) Mikata, Y.; Ohnishi, R.; Nishijima, R.; Konno, H. Fluorescent Detection of Phosphate Ion via a Tetranuclear Zinc Complex Supported by a Tetrakisquinoline Ligand and μ^4 -PO_4 Core. *Inorg. Chem.* **2016**, *55*, 11440−11446.
(71) Lovitt, J. I.; Hawes, C. S.; Lynes, A. D.; Haffner, B.; Mobius, M. E.; Gunnlaugsson, T. Coordination Chemistry of N-Picolyl-1,8-Naphthalimides: Colourful Low Molecular Weight Metallo-Gelators and Unique Chelation Behaviours. *Inorg. Chem. Front.* **2017**, *4*, 296−308.
(72) Gunnlaugsson, T. Supramolecular Pathways: Accessible Self-Assembly. *Nat. Chem.* **2016**, *8* (1), 6−7.
(73) Jones, C. D.; Steed, J. W. Gels with Sense: Supramolecular Materials That Respond to Heat{,} Light and Sound. *Chem. Soc. Rev.* **2016**, *45* (1998), 6546.
(74) Fang, W.; Liu, C.; Yu, F.; Liu, Y.; Li, Z.; Chen, L.; Bao, X.; Tu, T. Macroscopic and Fluorescent Discrimination of Adenosine Triphosphate via Selective Metallo-Hydrogel Formation: A Visual, Practical, and Reliable Rehearsal toward Cellular Imaging. *ACS Appl. Mater. Interfaces* **2016**, *8* (32), 20583−20590.
(75) Jung, S. H.; Kim, K. Y.; Lee, J. H.; Moon, C. J.; Han, N. S.; Park, S.-J.; Kang, D.; Song, J. K.; Lee, S. S.; Choi, M. Y.; Jaworski, J.; Jung, J. H. Self-Assembled Tb^{3+} Complex Probe for Quantitative Analysis of ATP during Its Enzymatic Hydrolysis via Time-Resolved Luminescence in Vitro and in Vivo. *ACS Appl. Mater. Interfaces* **2017**, *9*, 722−729.
(76) Bhattacharya, S.; Sengupta, S.; Bala, S.; Goswami, A.; Ganguly, S.; Mondal, R. Pyrazole-Based Metallogels Showing an Unprecedented Colorimetric Ammonia Gas Sensing through Gel-to-Gel Transformation with a Rare Event of Time-Dependent Morphology Transformation. *Cryst. Growth Des.* **2014**, *14* (5), 2366−2374.
(77) Ai, Y.; Li, Y.; Ma, H.; Su, C.-Y.; Yam, V. W.-W. Cyclometalated Platinum(II) Complexes of 1,3-Bis(1- *N* -Butylpyrazol-3-Yl)benzenes: Synthesis, Characterization, Electrochemical, Photophysical, and Gelation Behavior Studies. *Inorg. Chem.* **2016**, *55* (22), 11920−11929.

DOI: 10.1021/acs.cgd.8b00165
Cryst. Growth Des. 2018, 18, 4320−4333

(78) Samanta, S.; Dey, P.; Ramesh, A.; Das, G. A Solo Fluorogenic Probe for the Real-Time Sensing of SO_3^{2-} and SO_4^{2-}/HSO_4^- in Aqueous Medium and Live Cells by Distinct Turn-on Emission Signals. *Chem. Commun.* **2016**, *52* (68), 10381−10384.
(79) Kumar, R.; Sandhu, S.; Singh, P.; Kumar, S. Water Dispersed Fluorescent Organic Aggregates for the Picomolar Detection of ClO_4^- in Water, Soil and Blood Serum and the Attogram Detection of ClO_4^- in the Solid State by a Contact Mode Method. *J. Mater. Chem. C* **2016**, *4* (31), 7420−7429.
(80) (a) Haldar, R.; Rao, K. V.; George, S. J.; Maji, T. K. Exciplex Formation and Energy Transfer in Self-Assembled Metal−Organic Hybrid System. *Chem. - Eur. J.* **2012**, *18*, 5848−5852. (b) Prasad, K.; Haldar, R.; Maji, T. K. Rational design of a pyrene based luminescent porous Supramolecular framework: excimer emission and energy Transfer. *RSC Adv.* **2015**, *5*, 74986−74993.

DOI: 10.1021/acs.cgd.8b00165
Cryst. Growth Des. 2018, 18, 4320−4333